JOURNAL OF AIRCRAFT
Vol. 47, No. 3, May–June 2010

Design and Test of the UW-5006 Transonic Natural-Laminar-Flow Wing

Ubaldo Cella*
Piaggio Aero Industries, 80078 Naples, Italy
and
Domenico Quagliarella,† Raffaele Donelli,† and Biagio Imperatore‡
Centro Italiano Ricerche Aerospaziali, 81043 Capua, Italy

DOI: 10.2514/1.40932

A transonic natural-laminar-flow wing design procedure has been set up, integrating a parametric geometry model with several analysis tools. A direct design strategy has been applied and three levels of aerodynamic analysis have been used: a full-potential method (with which to rapidly iterate to obtain the target pressure distribution), an Euler solution coupled with a boundary-layer solver and a semi-empirical stability analysis method (for an intermediate evaluation that is able to include the laminar flow extension), and a full Navier–Stokes analysis with fixed transition (for a final verification of the design quality). A transonic natural-laminar-flow wing suitable for business aviation able to perform at least 40% of laminar flow in cruise with acceptable wave drag at Mach 0.78 has been designed and tested at flight Reynolds numbers. The laminar flow has been verified by infrared cameras.

Nomenclature

b	=	wing span
C_D	=	drag coefficient
C_{Dw}	=	wave drag coefficient
C_L	=	lift coefficient
C_p	=	pressure coefficient
c	=	chord
P	=	static pressure
S	=	reference surface
t	=	thickness
V	=	velocity
α	=	angle of incidence
Λ	=	sweep angle
ρ	=	density
τ	=	viscous stress tensor

I. Introduction

DURING the last decades, significant efforts have been addressed to research in laminar flow technology, both hybrid and natural. Several research projects financed by the European Commission (ELFIN I and II, LARA, HYLDA, HYLTEC, and ALTTA) evidence how strong the interest is in aeronautics about laminar flow technology.

The work described in this paper was developed within the Italian VITAS research project, which had the objective to acquire knowledge, develop tools, and define new technologies for the design of an innovative transport aircraft. The well-known benefits in terms of friction drag reduction derived from the development of extended regions of laminar flow over the wetted surfaces of aircraft were convincing enough, together with the past European Union research project experience, to dedicate a substantial part of the project to the investigation of the practical feasibility of such technology in the range of speed of modern business aviation. To this aim, several steps were scheduled: development and assessment of numerical tools, optimization and testing of a 2-D section, extension of the experience to the 3-D design of a swept natural-laminar-flow (NLF) wing, and verification of the laminar flow extension at flight Reynolds and Mach numbers in a high-speed wind tunnel. This paper details the three-dimensional design phase and summarizes the results of the tests performed in the German–Dutch wind tunnel, DNW-HST.

The paper is divided into three parts:

1) The targets of the design are first listed, referring to a medium-sized business jet. The aerodynamic tools and the design methodology are described, detailing the philosophy of the main wing-section design and reporting the three-dimensional design strategy with its constraints and solutions.

2) The second part is dedicated to the postdesign numerical verification. Several Navier–Stokes runs and stability evaluations are reported to verify the quality of the design.

3) The wind-tunnel test setup and the comparison between theoretical and experimental solutions are reported in the third part of the paper.

II. Wing Design

The design of an aircraft is the resulting combination of the work produced on several subjects (structures, avionics, plants, and aerodynamics) that progress in parallel on the same object. Each of them has different, and often conflicting, requirements. The aerodynamic targets of a wing are usually revised during the predesign phase to meet the requirements of other groups, in some cases leading to compromising solutions that are either not acceptable or not interesting for the market.

The objective of this work is not only to create a purely research wing that is able to exhibit a significant extension of laminar flow, but it also demonstrates the feasibility of the NLF technology within the integrated design process of the aircraft. Because the wing must fulfill the requirements derived from other areas of study, the aerodynamic design was performed in parallel with the predevelopment activity, wing-box structure definition, plant installation, and manufacturing methodology study.

The design refers to a family of business jets for which the weight and selected flying conditions require wing target performances across a large spectrum of aerodynamic conditions.

Received 10 September 2008; accepted for publication 24 February 2009.

*Senior Research Engineer, Piaggio High Technology.
†Senior Research Engineer, Applied Aerodynamics Laboratory.
‡Head, Transonic Testing Group.

Table 1 Aerodynamic design targets of the wing

Design point	Mach	Reynolds	C_L	C_M	Transition	C_{Dw}
Long-range cruise 1	0.75	8.3×10^6	0.5	> -0.11	$>40\%c$	0
Long-range cruise 2	0.75	8.3×10^6	0.4	> -0.11	$>40\%c$	0
High-speed cruise	0.78	8.7×10^6	0.46	> -0.13	$>40\%c$	<0.002
Climb	0.7	$>10 \times 10^6$	0.6	——	$>20\%c$	0

A. Design Targets and Constraints

The selected design points derive from long-range cruising, high-speed cruising, and stall requirements. An additional design point regarding the climb condition has been added with lower priority. A range of possible weights and operative altitudes has also been considered that cause the wing to exhibit the required laminar extension and wave drag in a range of the cruising polar curve instead of at a single design point, but in a range of the cruising polar curve. Table 1 summarizes the selected design requirements.

Figure 1 depicts a sketch of the wing planform. It is a tapered sweptback wing with aspect ratio of 8 and taper ratio of 0.34. The leading-edge sweep angle was 20 deg. Such a value is considered, from the experience of the ELFIN flying tests, to be a limit for the crossflow stability of the boundary layer [1]. The wing is mounted below the fuselage. A dihedral angle of 2 deg was adopted.

For structural reasons and to maintain the fuel-storage capability of the wing box, the root section has a minimum thickness requirement that, considering the reference-surface planform chord (gray lines of Fig. 1), would correspond to a too-high value of thickness-to-chord ratio (dotted curve of Fig. 2). To avoid strong compressibility effects in this region, the root chord was extended. With this solution, the root t/c value was reduced (solid curve of Fig. 2). The inner trailing edge is smoothly jointed to the outer trailing edge of the wing, which is kept straight from this point.

Particular attention should be paid to the assembly of the wing box. Laminar flows require a very high level of surface smoothness without any visible excrescence (rivets, screws, gaps, etc.). A hypothesis is to adopt the well-tested constructing methodology of the Piaggio P180 Avanti. In this case, the ribs and the spars are riveted to the integrated stringers of panels obtained by machining a thick aluminum block. To limit the quantity of the raw material, such panels should be as flat as possible (Fig. 3). This is a severe constraint in the choice of the twist and thickness distribution and, in particular, it conflicts with the necessity of having thick cambered airfoils on the outer part of the wing (to reach high values of maximum lift), thin airfoils in the inner part (to contain the wave drag at high speed), and thick root sections (for the mentioned structural and fuel-storage reasons).

The composite forming of the panels would significantly relax the geometric constraints. It was, however, preferred during this phase to adopt a traditional metal technology and for the quantification of the advantage in adopting a composite wing box to be deferred to future activities.

B. Three-Dimensional Aerodynamic Design

With so many imposed constraints, aerodynamic targets, and project variables, a direct design strategy was preferred to an automated multi-objective optimization procedure. The wing geometry was built from six airfoil sections. Particular care in the generation of the airfoil spline curves is necessary for both aerodynamic (aerodynamics are sensitive to the second derivative of the geometry) and CAD modeling reasons (generation of smooth and regular 3-D model surfaces). Several sections must also be derived from a similar shape to avoid deformation of the surface. This requirement obviously conflicts with the different aerodynamic target of the various regions of the wing. Simply put, the aerodynamic design and the CAD geometry construction are strictly related and constrained each other.

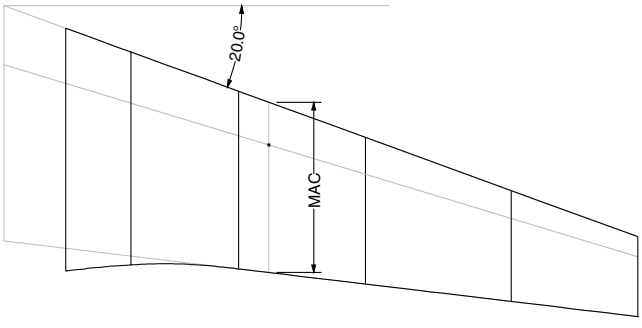

Fig. 1 Wing planform.

The main variables of the design are the positions of the six control sections and their thicknesses, the local twist, and the airfoil geometry. A typical design iteration starts with a first hypothesis of twist, thickness, and relative lift coefficient distribution.[§] The airfoil modification follows with a nonviscous three-dimensional approach (full-potential method). Refinement of the airfoils consists of a more accurate viscous two-dimensional design of the airfoils by applying the *rule of cosine* (using a coupled Euler/boundary-layer code [3]). This phase is essentially performed with a 2-D inverse strategy. A three-dimensional verification using a 3-D Euler code coupled with a boundary-layer code and a semi-empirical stability analysis method (database) follows. This analysis is the first confirmation of the stability of the three-dimensional laminar flow in the presence of crossflow instability. The geometry must now be built and adjusted by CAD. If it satisfies the geometry requirements, a complete 3-D viscous Navier–Stokes verification concludes the iteration.

1. *Thickness Distribution*

The selection of the thickness distribution along the span is a compromise between several requirements. The highest bending moment of the wing is located at the root, which should then be as thick as possible. Thickening the root also greatly increases the fuel-storage capacity of the wing box. Moreover, the storage of the main landing gear is usually located in this region, which very often represents the first constraint for the structure. Increasing the thickness, however, strongly conflicts with the high-speed performance requirement of the mission (the wave drag effects grow approximately with the fourth power of the thickness-to-chord ratio). A drastic reduction of the thickness, moving away from the root, is then desirable. Relatively high thickness values are again required on the tip region to maintain acceptable low-speed performance. In conclusion, an ideal thickness-to-chord ratio distribution is characterized by a very thick root airfoil followed by a strong spanwise thinning and proceeding with a relatively constant value. The surface development of such a wing will generate wing-box panels highly cambered in the spanwise direction. Such a solution is not ideal for the manufacturing methodology adopted (too much raw material). Single curvature panels, however, would force the geometry to have thinner root and tip sections (dashed curve in Fig. 2). A compromising solution (very common on commercial aircraft) is to introduce a kink in the inner part of the wing by increasing the chords of the root region. The solution adopted in the present design allows the same root box thickness to be kept and to reduce the thickness-to-chord ratio.

2. *Twist Distribution*

The spanwise load on the wing is primarily controlled by the twist and by the airfoil geometry (camber). It particularly affects the

[§]The philosophy of the design, in terms of compromising target pressure distribution at several design points, has been previously investigated by a 2-D multi-objective numerical optimization using genetic algorithm [2].

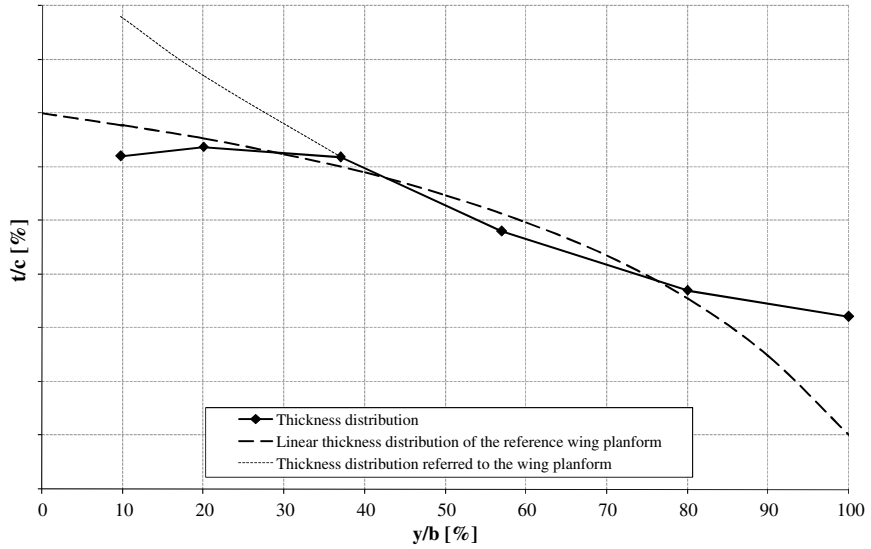

Fig. 2 Thickness distribution.

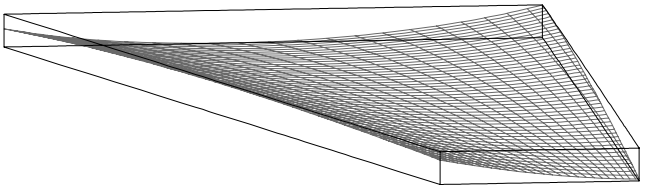

Fig. 3 Source material block required for panel machining (example without stringers).

induced drag (vortex drag), which must, however, be evaluated in the complete aircraft configuration [4]. The ideal minimum vortex drag is achieved when the load distribution of the aircraft is elliptic (including fuselage, nacelles, and tail load). This generally means, considering the trimmed configuration with a negative lift tail, a non-elliptic-wing load with some inboard loading [5]. Such a load distribution has several advantages: it has a positive effect on the pitching moment (for sweptback wings) and consequently on the trim drag; it permits lower weight for the wing structure [6]; and it reduces the risk of tip stall at low speed. The latter aspect is particularly critical for sweptback wings, for which the vortices generated by the inner load gradients have the tendency to increase the lift on the outer regions. Furthermore, the thinner tip sections together with their lower Reynolds numbers force the use of higher cambered airfoils and require a particularly accurate design to meet the clean-wing stall pattern target. All of these aspects lead to high values of wing twist. Figure 4 reports the selected spanwise twist distribution.

3. Airfoil Design

The thickness and twist configuration of the wing must be defined in parallel with the design of the airfoils, which in turn must satisfy the local geometric and aerodynamic requirements. In the root region, the flow is strongly three-dimensional. The pressure isolines are forced to be orthogonal to the symmetry plane, causing a loss of pressure close to the nose (and consequently a lift loss) and amplifying the wave drag (with respect to the two-dimensional characteristics of the airfoil) [7]. In this area, a strong three-dimensional flow soon turns (after the first 10–15% of the exposed semispan) to the more characteristic pressure distribution of the wing. The use of at least two control sections is necessary here.

The airfoil designed for the central region will be the driving airfoil responsible of the aerodynamic performance of the wing and will characterize its design philosophy. All of the other sections should refer to this airfoil (in both a geometric and aerodynamic sense) and

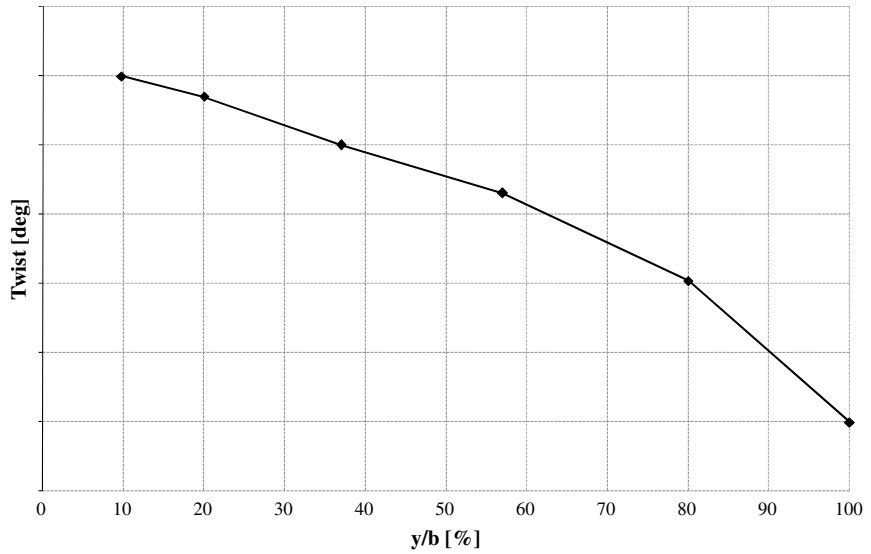

Fig. 4 Twist distribution.

should be modified to meet the local requirements. The tip region must be designed with reference to the low-speed requirement constraints. The extreme tip will also generate a strong three-dimensional flow, and therefore two control sections are required in that region. With this vision, at least five sections are necessary to build the wing. A sixth section permits achieving better control of the geometry, but it is generally suggested to not exceed this number.

Three main airfoils have been designed: a base airfoil located at 37% of the semispan, a tip airfoil that defines the aerodynamics in the region of the aileron, and a root airfoil located in the aerodynamic symmetry plane of the wing, which was designed completely in 3-D. The six control sections are derived from these three airfoils by scaling or combining them as required.

C. Transonic Laminar Airfoil Design for a Swept Wing

Natural laminar airfoil design strategy conflicts in several aspects with supercritical design. For stability reasons, a continuous streamwise decrease of pressure must be present. For two-dimensional flows, the stability of the laminar boundary layer is roughly proportional to the pressure gradient and inversely proportional to the distance from the stagnation point [8]. The physics of this phenomenon are dominated by the propagation of the so-called Tollmien–Schlichting instability [9]. A similarly shaped pressure profile would lead to aft pressure values (high local Mach numbers), which restore higher pressure through a relatively strong shock. If a low-drag profile in high speed is required, particular attention must then be paid to the selection of the target compromise pressure distribution. In the case of a sweptback wing, the three-dimensionality of the flow induces another instability type (crossflow) that, contrary to the Tollmien–Schlichting instability, has a great evolution in the region of the leading edge. Its importance grows with the sweep angle.

In this work, the airfoils have been analyzed using a so-called quasi-3-D approach. The inviscid pressure distribution of the considered section, derived from a 3-D analysis of the wing, is used to calculate the local boundary layer. The method (also known as the Kaups–Cebeci approach [10]) is based on the conical-flow assumption, which consists of analyzing the airfoil section of a wing modeled as a cone (the twist is neglected) for which the generators pass through the provided airfoil geometry. The root and the tip airfoils are similar and simply scaled. The boundary-layer equations are transformed in conical coordinates and solved along the arc obtained from the intersection of the wing with a sphere for which the center is the origin of the wing generators. This approximation permits obtaining a 3-D solution of the boundary layer of a swept tapered wing, solving a form similar to two-dimensional boundary-layer equations.

The transition location is estimated using the database method. The principle is to simplify the stability analysis by an analytical representation of the growth rate of the disturbances as a function of certain relevant boundary-layer parameters [11]. The analytical correlations have been obtained by an accurate investigation on the growth rates of the disturbances computed using methods based on the linear stability theory for a particular airfoil: the ONERA D profile.

The operating conditions (lift coefficient and Mach and Reynolds numbers) and the target compressibility drag of the airfoil to be designed in two dimensions are obtained by referring to the rule of cosine [12] (see Appendix A).

1. *Base Airfoil Design*

The design of the main airfoil takes into consideration three configurations: climb, long-range cruise, and high-speed cruise. From preliminary design activity, the following 2-D design points were defined:

1) Climb is at Mach $= 0.7$ and $C_l = 0.7$.
2) Long-range cruise is at Mach $= 0.75$ and $C_l = 0.62$.
3) High-speed cruise is at Mach $= 0.78$ and $C_l = 0.58$.

Each region of the airfoil influences particular aspects of the design. The final geometry must generate optimal pressure distributions at the three design conditions, thus accomplishing the required tasks.

In Fig. 5 an example of the pressure distributions generated by the same geometry at the three design conditions is plotted. The figure highlights how several characteristics of the design can be circumscribed into areas of influence. In more detail, the leading edge of the airfoil is the region of the development of crossflow instabilities. A steep pressure gradient is (in general) required here. If an amount of laminar flow is required in climb condition, a sufficient plateau must be present after the stagnation region. This requirement limits the value of C_P that can be reached locally and imposes a kind of round shape of pressure distribution in cruising condition that causes lift reduction and introduces further stability constraints in the following region. For this work, a compromising target of 20% of laminar flow in climb condition was defined.

The laminar extension in cruise condition must be higher than 40%. The pressure distribution in the Tollmien–Schlichting-dominated instability region is then constrained by the stability requirements of the boundary layer. The following region (up to the pressure recovery region) should be approached with a supercritical design methodology [13], in which a design aimed at the generation of a relatively weak shock in high speed will develop a second recompression structure in cruise (double shock). The last 30% of the upper surface is devoted to recovering a pressure as close as possible to the stagnation value. The shape of the pressure rise must be defined by investigating the separation limit of the boundary-layer using viscous tools. A rough indication of the separation margin is the local value of the shape factor. A design with a constant value of the shape factor up to the trailing edge will delay the separation but will lead to a sudden stall of the entire recovery region, evidencing a discontinuity in the lift curve of the airfoil at high incidences.

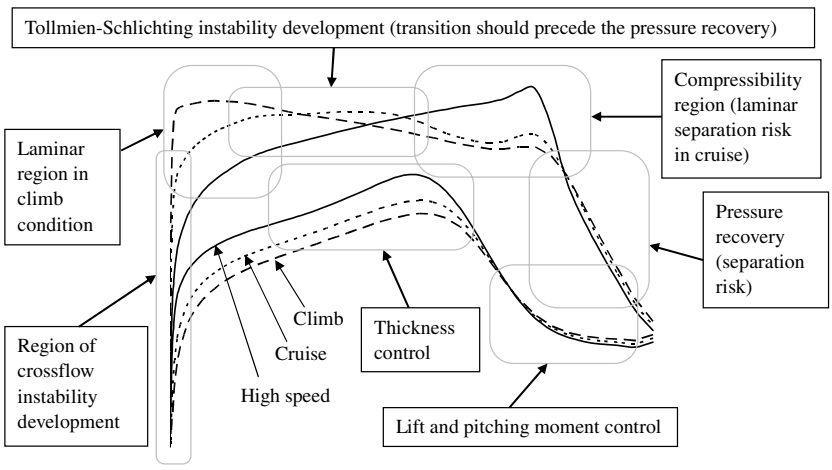

Fig. 5 Typical pressure development at the three design conditions by the same geometry.

The lower pressure distribution can be split in two regions. The first part (usually up to around 60% of the chord) is strictly related to the thickness of the airfoil. It is important, however, to be careful when exceeding the critical C_P to not generate further shocks, which might cause drag increase at offdesign conditions. The rear lower part of the airfoil can be used to trim the lift coefficient. Two critical aspects are associated with this region. For thick geometries, the pressure recovery can be very strong, causing separation; in addition, high pressure values here strongly contribute to increase the nose-down pitching moment.

2. Root Airfoil

In the case of a swept wing, the two-dimensional approximation is not valid for the section on the symmetry plane. The design of this airfoil must be performed by verifying the complete three-dimensional solution and should be oriented to the generation of a pressure distribution, which minimizes the difference with the wing design philosophy and then reduces its influence on the other parts of the wing. Such geometry will be significantly different from the other airfoils. The nose region will evidence a nose-up shape and the upper surface will be very flat up to the trailing edge. The camber will then generally be negative and the airfoil must be set with a relatively high angle of incidence to recover the local lift loss.

3. Tip Airfoil

The design of the tip geometry is driven by the stall requirement of the wing. When the inner region begins to separate, the aileron region must maintain the lift without separation and, in any case, the stall must start as close as possible to the root of the wing.

Sweptback wings are overloaded in the tip region, and therefore a reduction of the tip chord is necessary. Moreover, the lower Reynolds numbers and the smaller thickness-to-chord ratios do not permit stall at the root without twist values that strongly penalize the wing performances at other flying conditions. For this reason, the tip geometry design must be oriented toward the maximum lift optimization, being careful to control the load of the rear part of the airfoil (to limit the aileron hinge moment).

To design an airfoil with the aim of improving the maximum lift without increasing the zero-incidence lift means focusing the attention particularly on the leading-edge geometry. A first rough indication of the airfoil stall limit can be obtained by evaluating the minimum value of pressure coefficient reached at high incidence. The order of critical values is between 10 and 13. The geometry oriented to the minimization of the pressure peak has a drop nose shape (high camber in the leading-edge region) with low values of the curvature. The first impact of this characteristic in the other design conditions is a reduction of the nose pressure gradient, reducing the crossflow stability of the boundary layer.

III. Postdesign Analysis

The performance of the wing has been verified by a 3-D Navier–Stokes analysis using the Centro Italiano Ricerche Aerospaziali ZEN (zonal Euler Navier–Stokes) code. ZEN is a 3-D Reynolds-averaged Navier–Stokes finite volume code using multiblock structured grid [14]. Several computations have been performed with the transition fixed to maintain 40% of laminar flow on both sides of the wing. The performances in the case of fully turbulent flow have been also verified. The solution presented in this paper has been obtained using the k-ω shear-stress-transport turbulence model.

The grid was generated using the ANSYS ICEM/CFD (computational fluid dynamics). It is a structured multiblock mesh with 2.8 million hexahedral cells (Fig. 6). The far field is extended 50 chords away from the wing in all directions. The boundary layer is solved up to the wall. The closest layer of cells on the surface is located at a $Y+$ distance on the order of 1. There are 244 cells clustered on the airfoils, 40 on the thick trailing edge, and 80 in the spanwise direction.

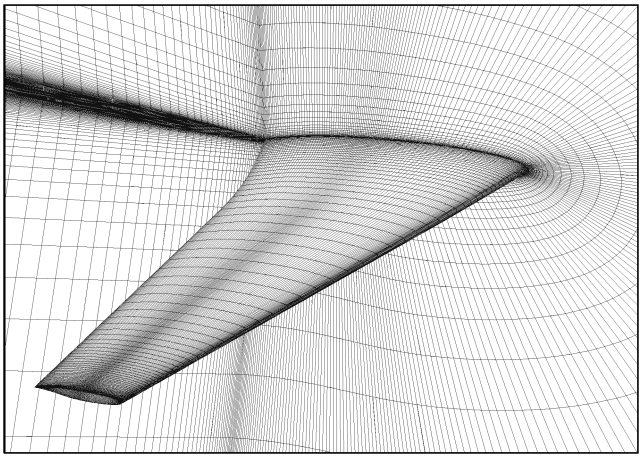

Fig. 6 Navier–Stokes computational domain.

A. Navier–Stokes Solutions

Figures 7 and 8 compare the two-dimensional viscous pressure distribution in long-range and high-speed cruising conditions (computed by the MSES code) with the three-dimensional Euler and

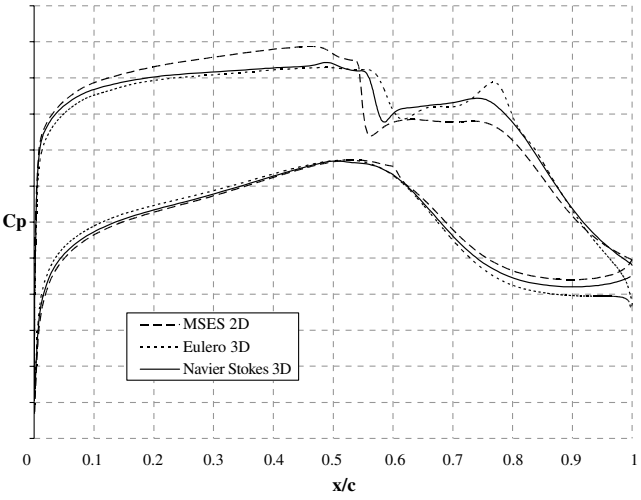

Fig. 7 Base airfoil design verification in long-range cruising condition (transition at 40%c).

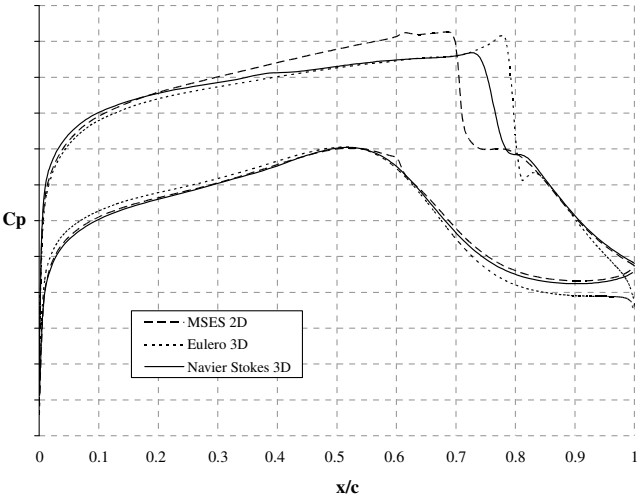

Fig. 8 Base airfoil design verification in high-speed cruising condition (transition at 40%c).

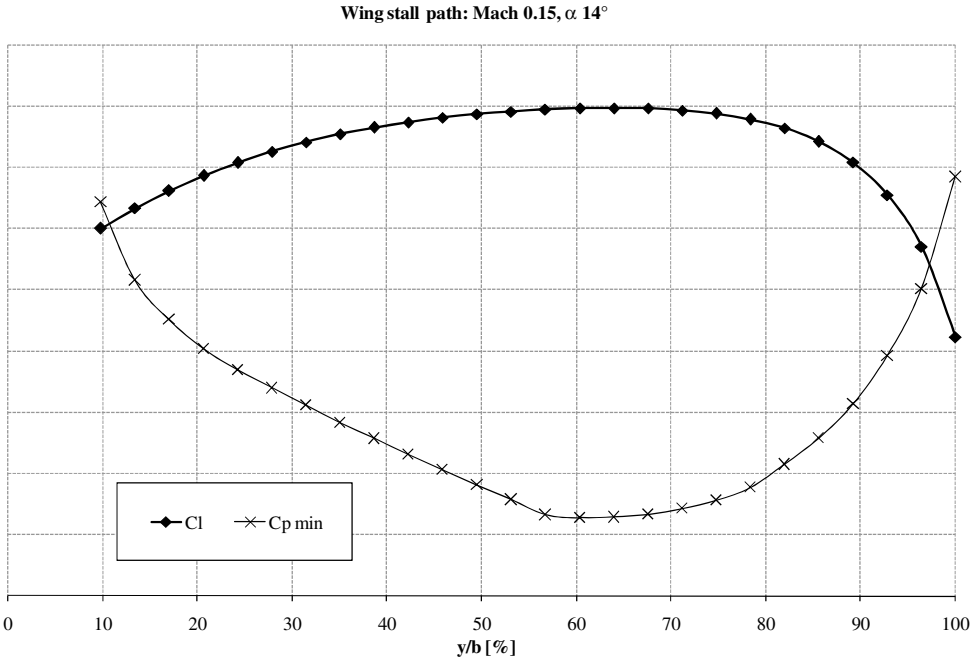

Fig. 9 Stall path of the wing (full-potential solution).

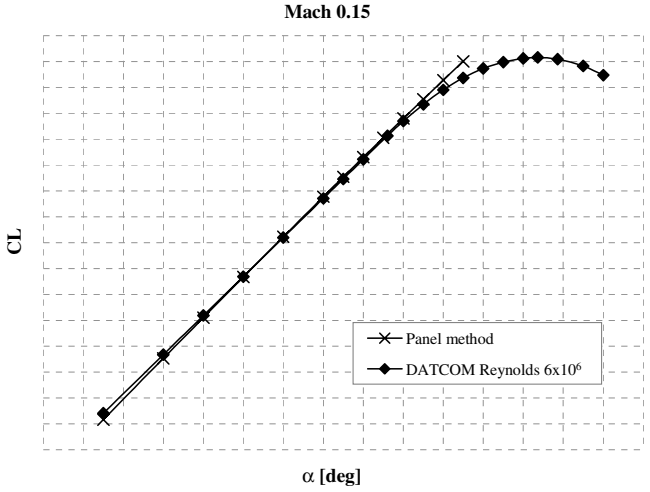

Fig. 10 Maximum lift estimation of the wing.

Navier–Stokes solutions. The two 3-D solutions are very similar except in the compressibility region. The discrepancies between the 2-D and 3-D pressure distributions are related to the limit of the rule of cosine (which is valid for infinite-span wings) and to the value of the sweep angle used, which is higher than the aerodynamic sweep angle.[¶]

The computed wing drag rise at $C_L = 0.5$ passing from Mach 0.6 to 0.75 is only one drag count, and it is 19 drag counts passing from Mach 0.6 to 0.78. The drag rise at $C_L = 0.46$ and Mach 0.78 is 13 drag counts, well below the target limit. The drag rise in the case of fully turbulent flow was also evaluated, confirming the target value of 20 drag counts at $C_L = 0.46$. The moment coefficient at Mach 0.75 is -0.073 and -0.07 at Mach 0.78, also well below the target limit in this case.

[¶]The airfoil commonly considered for a two-dimensional analysis of a finite swept tapered wing is the section with the plane orthogonal to the sweep angle at 25% of the chord. In this work, the angle used in the application of the rule of cosine is the leading-edge sweep angle. This choice is justified by the necessity of having higher accuracy in the region of crossflow instability development.

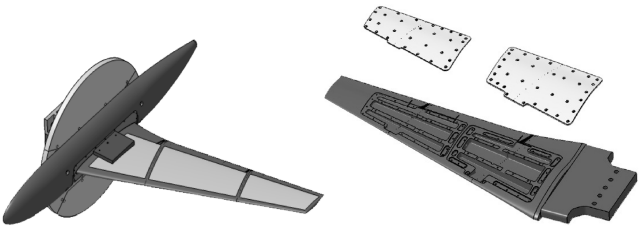

Fig. 11 Detail of the CAD model assembly.

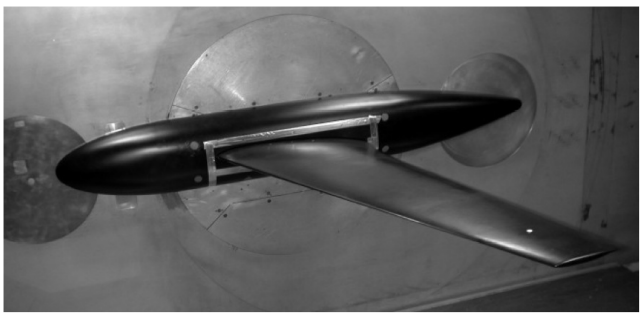

Fig. 12 UW-5006 NLF wing/fuselage model installed in the wind-tunnel test section.

B. Low-Speed Performances

The stall characteristics of the wing have been evaluated with the DATCOM code [15]. This method, based on empirical formulations, is used for preliminary design purposes. It evaluates the 3-D lift curve

Table 2 IR test points

Mach	Reynolds	C_L
0.75, 0.78	4×10^6	0.4, 0.45, 0.5, 0.55
0.6, 0.7, 0.75, 0.78, 0.8	8×10^6	0.4, 0.45, 0.5, 0.55
0.6, 0.7, 0.75, 0.78, 0.8	10×10^6	0.4, 0.45, 0.5, 0.55

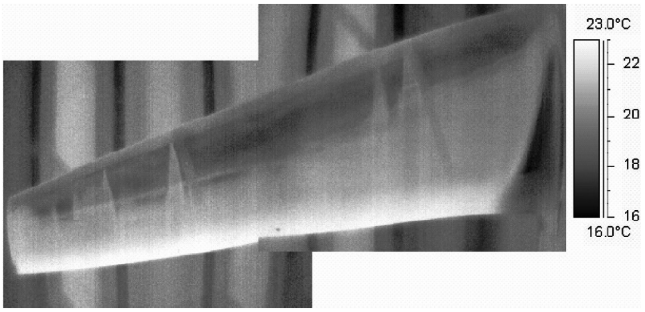

Fig. 13 IR image at $M = 0.75$, $Re = 8 \times 10^6$, and $C_L = 0$.

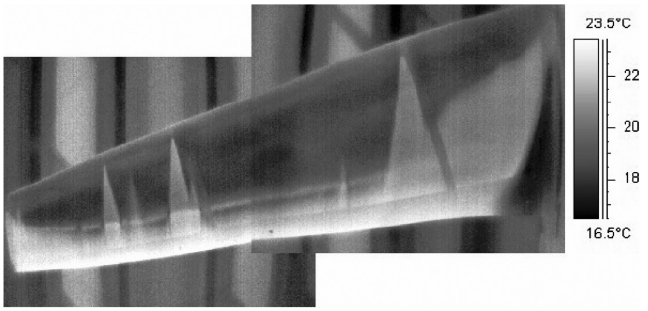

Fig. 14 IR image at $M = 0.78$, $Re = 8 \times 10^6$, and $C_L = 0.45$.

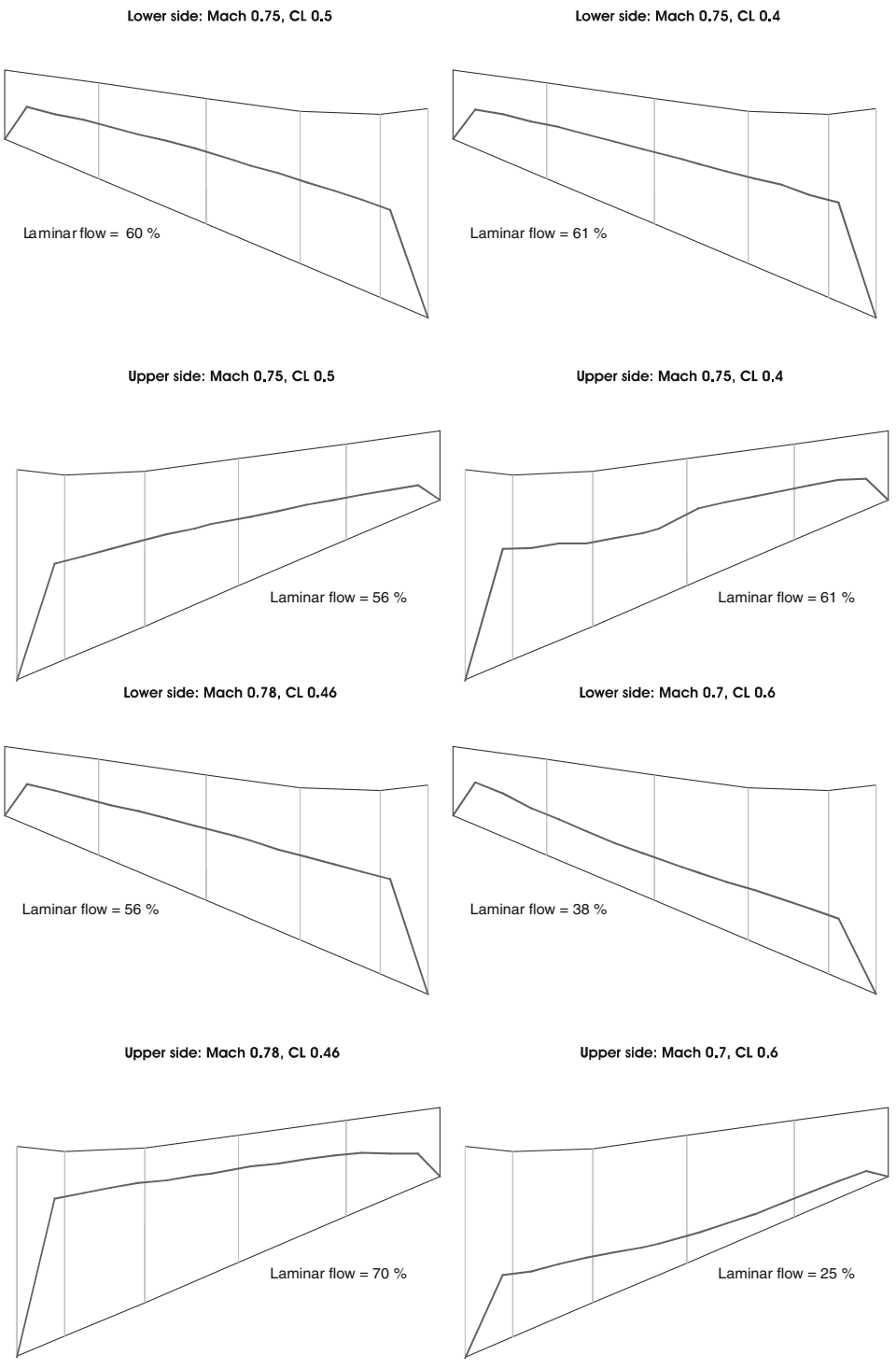

Fig. 15 Computed transition locations (database solution).

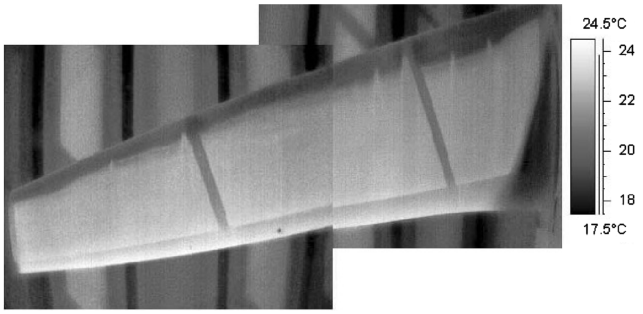

Fig. 16 IR image at $M = 0.7$, $Re = 10 \times 10^6$, and $C_L = 0.55$.

and the maximum lift using the geometrical data of the wing and a provided reference-airfoil low-speed lift curve.

In addition, the lift curve has also been computed using a panel method. The upper limit (maximum lift) refers to the case in which a pressure coefficient value of −13 is first reached somewhere on the wing (Fig. 9). The DATCOM and the panel solutions are plotted in Fig. 10. Both methods predict a maximum lift of 1.3.

IV. Wind-Tunnel Test Campaign

To check the performance of the newly designed laminar wing, a wind-tunnel test campaign in the transonic regime at flight Reynolds numbers was carried out on a 1:6 half-wing scaled model in the DNW-HST facility in Amsterdam. Particular attention was paid to designing a support solution that is able to reduce the interaction between the wing and the tunnel wall boundary layer. A proper fairing, not weighted by the side-wall balance, used to move the model out of the test-section wall boundary layer was designed and manufactured. Its shape also had to ensure that the load distribution on the model was representative of the isolated wing and that leading-edge contamination was avoided.

A. Test-Rig Configuration

All model design activities [3-D CAD model, finite element method (FEM) analysis, cable routing simulation, etc.] were performed using the CATIA version 5 computer-aided engineering and CAD integrated system. The model is made of a one-piece machined main element, including an integrated mounting interface, and is equipped with two cover panels located on the bottom side (Fig. 11). A safety factor of 5, with reference to the maximum expected loads based on FEM analysis, was required. The FEM solution showed a deflection at the model tip lower than 30 mm and a rotation angle lower than 0.5 deg under the maximum expected load conditions.

The model was equipped with 129 pressure taps located along two chordwise stations at 30 and 70% of the span. A 0.25 mm tap diameter was selected to avoid any contamination of the laminar boundary layer. Five high-frequency pressure transducers were also installed on the model.

Low-thermal-conductivity panels to be installed on the upper side of the wing facilitated the use of the infrared thermography technique. The panel thickness dimensioning is related to the sensitivity of the thermocameras used for wind-tunnel measurements. Based on previous experience of the DNW wind-tunnel experts, a thickness of 2.5 mm was identified as sufficient to guarantee a correct measurement. To realize the panels, three dedicated big pockets with a constant depth of 2.5 mm were machined on the upper surface of the main model element. The pockets were successively covered with stainless-steel-filled epoxy putty (Devcon). Such material has sufficiently low thermal conductivity to be machined together with the steel surfaces. After the putty had completed the hardening process, the external model surface was finished by machining the whole assembly. After the painting process and hand-finishing, a surface roughness value lower than 0.8 μm was achieved (the displacement thickness in the first 5% of the chord should be higher than 10 μm).

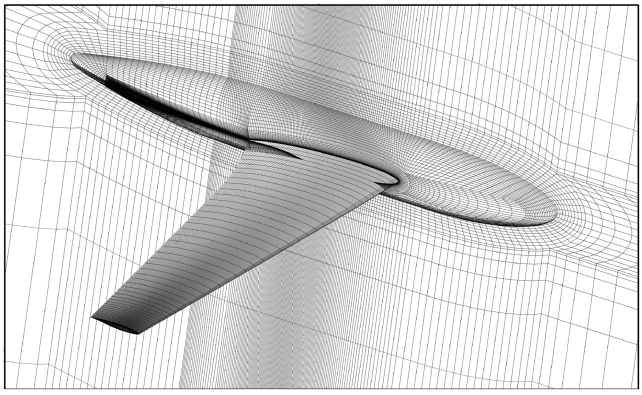

Fig. 17 Numerical domain in the wind-tunnel configuration.

B. Test Results

The HST is a variable-density closed-circuit wind tunnel. An adjustable nozzle is followed by a test section with solid side walls and movable slotted top and bottom walls (about 12% open per wall). Top and bottom walls can be adjusted to obtain a test-section height of 1.60 or 1.80 m. An excellent flow quality is achieved by a high contraction ratio of 25 at a test-section height of 1.6 m and a contraction ratio of 22.2 for a test-section height of 1.8 m. The UW-5006 NLF wing tests were performed at a test-section height of 1.8 m to reduce the wall interference as much as possible. Figure 12 shows the installation of the model in the test section.

The test campaign was aimed primarily at the confirmation of the wing design quality in terms of laminar flow characteristics. The transition position on the upper side of the wing was evaluated using an infrared thermography technique. The flow visualization was performed using two Thermovision A40M infrared cameras. The image resolution of both cameras was 320×240 pixels. Special glass windows coated for infrared (IR) measurements were mounted on the tunnel ceiling slats.

As summarized in Table 2, the selected test conditions for the IR visualizations covered the cruising design points of the wing in terms of Mach number and C_L, as well as several points at offdesign conditions.

Figures 13 and 14 show the results of the transition visualization obtained, respectively, at Mach numbers of 0.75 and 0.78 at $Re = 8 \times 10^6$ (long-range and high-speed cruise). The region in which the flow is laminar appears colder than in the turbulent region. This is due to the lower heat transfer that occurs in laminar flows. In other words, the air, which has a temperature higher than the wing, warms up the model more in the turbulent region than in the laminar region. In the figures, the laminar regions are darker than the turbulent regions. Two main turbulent spots are present, starting from the pressure taps on the leading edge. These spots were present in all of the tests performed. Other occasional spots appeared with the rise of Reynolds number. At $M = 0.78$ a successful extension of natural laminar flow was obtained on the model upper surface up to 70% of the chord length, whereas the laminar extension at $M = 0.75$ was around 40% of the chord (Fig. 15). In the central and outer parts of the wing, the laminar flow extends up to the shock wave position. In the region close to the root, the laminar flow is lower than expected.

In Fig. 16 the IR image at Mach = 0.7, Reynolds = 10×10^6, and $C_L = 0.55$ is reported. This condition refers to the climb design point, but at a lower lift. The target of 20% of laminar flow was not reached.

C. Comparison with Numerical Solutions

The infrared visualizations evidenced a laminar flow extension in the design points that was slightly lower than expected, particularly at the root region of the wing. A first hypothesis was to ascribe this failure to an insufficient accuracy of the model geometry in the region of the Devcon material. Slight waviness was, in fact, noticed in the

upper surface of the wing, which might be responsible for an irregular pressure distribution. To investigate this and other aspects, a CFD test session was planned on a new numerical configuration built by generating the computational domain on the model geometry measured after the manufacturing process. A new mesh including the fairing, as in the wind-tunnel configuration, was used (Fig. 17). Fully turbulent calculations using the CFD + + commercial code using the two-equation k-ω turbulence model were run. The analysis was performed at the two main design points: Mach 0.75 with C_L 0.5 and Mach 0.78 with C_L 0.46.

In Figs. 18 and 19 the computed surface pressure coefficient, respectively, for the theoretical designed wing and for the measured wind tunnel model, is reported together with the C_P plot at several sections in cruise and in high-speed conditions. From Figs. 20–23 the

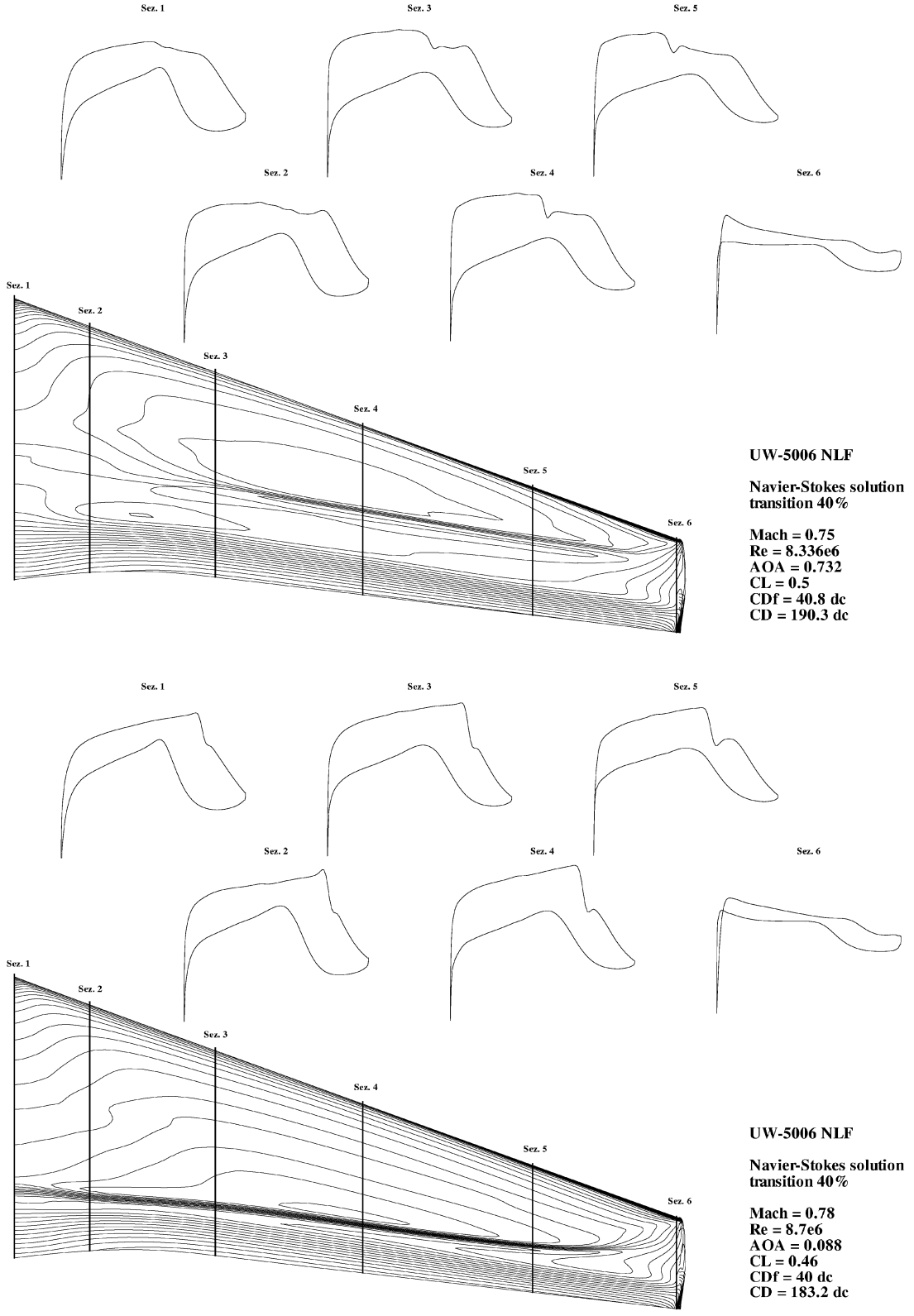

Fig. 18 Three-dimensional Navier–Stokes pressure distribution (transition at 40%).

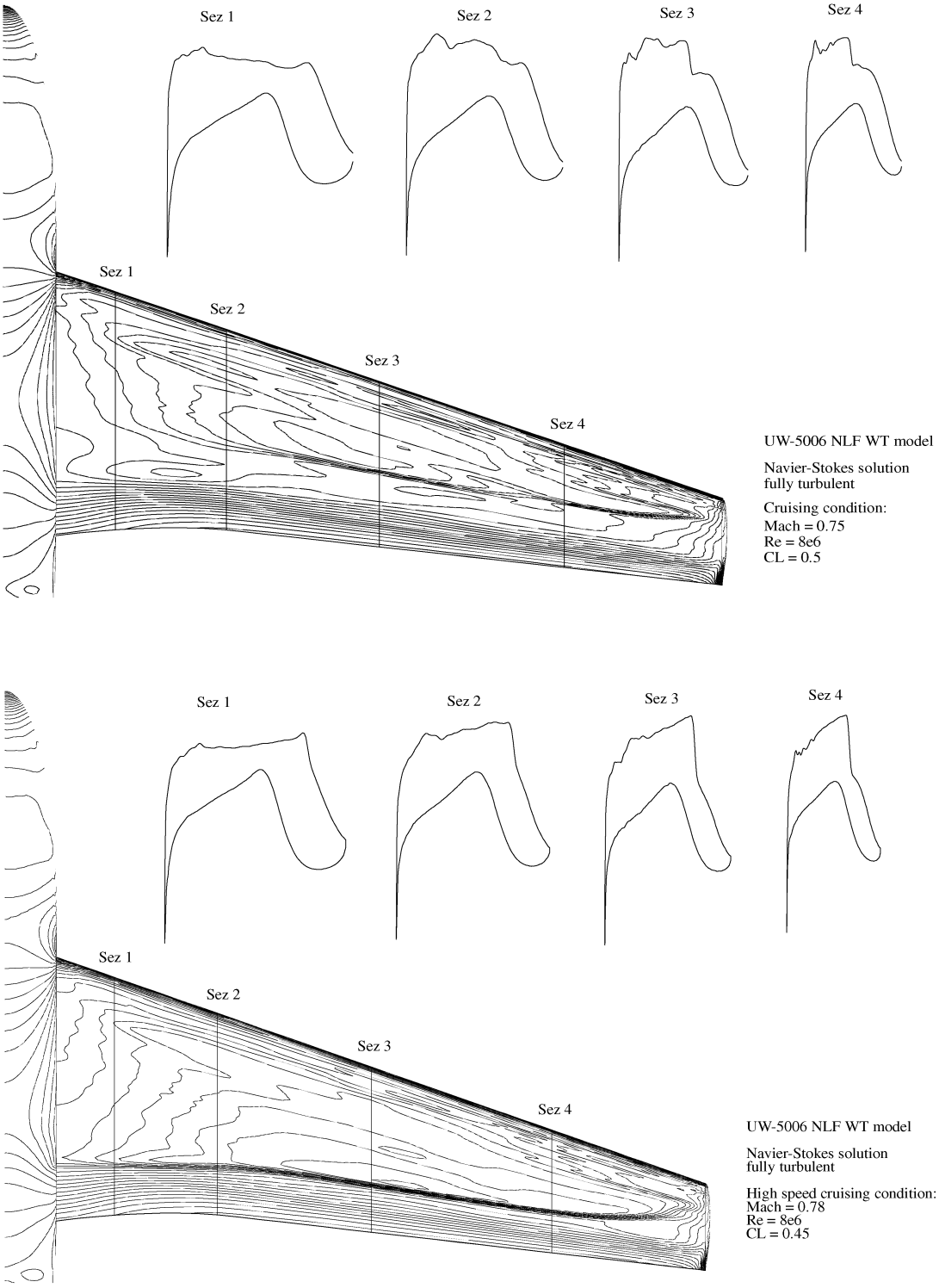

Fig. 19 Three-dimensional Navier–Stokes pressure distribution of the wind-tunnel model.

experimental pressure measurement for both laminar and turbulent cases is compared with the numerical solutions.

The irregularity of the geometry is reflected in both the numerical and experimental pressure distributions. The laminar flow, however, appears to tolerate such surface waviness. There is also a disagreement in the angle of incidence between the experimental and the numerical solutions, caused by the wind-tunnel wall interference.

The influence of the nature of the boundary layer on the recompression structure is evident by comparing the two experimental laminar and turbulent measurements. The position of the recompression in the case of laminar flow is moved aft with respect to that developed by the turbulent flow, giving the possibility of generating the same lift at lower incidence. This behavior permits the laminar flow to also benefit in terms of compressibility performance. The position of the shock with fully turbulent flow is not confirmed by the numerical solution, which estimates a stronger and more aft recompression than experiments at Mach 0.78 in both stations. The reason for laminar flow loss in the inner region of the wing is explained by the numerical solution, because in both cruise and high-speed conditions, the streamwise pressure gradient close to the wing root is more unfavorable than the theoretical design target.

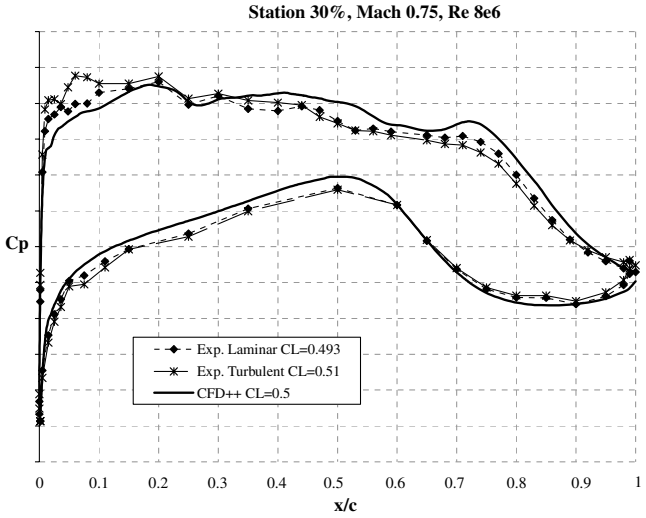

Fig. 20 Numerical and experimental pressure in long-range cruising condition at the inner pressure tap station.

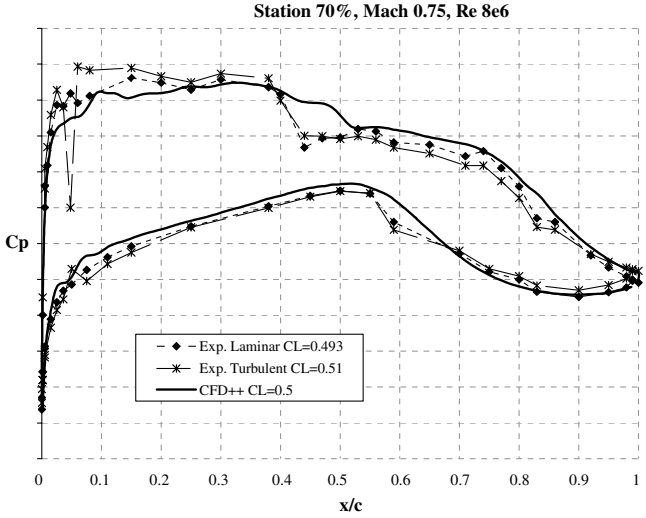

Fig. 21 Numerical and experimental pressure in long-range cruising condition at the outer pressure tap station.

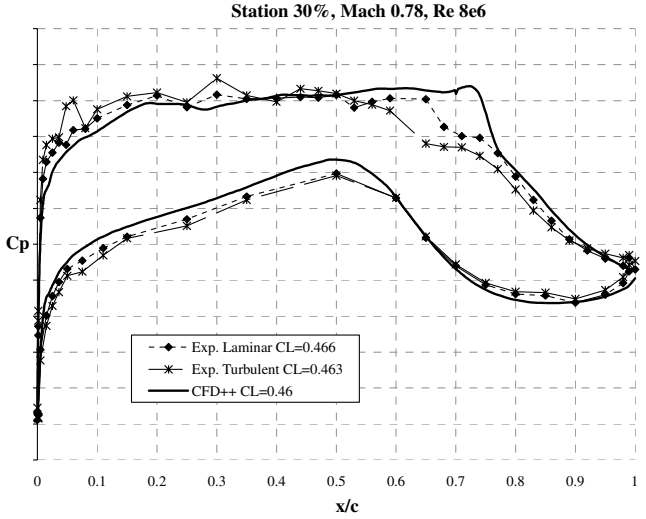

Fig. 22 Numerical and experimental pressure in high-speed cruising condition at the inner pressure tap station.

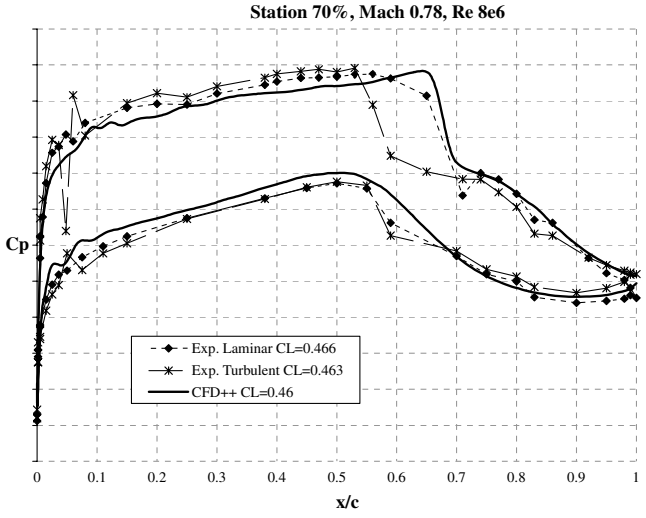

Fig. 23 Numerical and experimental pressure in high-speed cruising condition at the outer pressure tap station.

V. Conclusions

A transonic natural-laminar-flow wing has been designed using a direct strategy. The geometry refers to a medium-sized business-jet-class aircraft. The target design conditions selected are climb, long-range cruise, and high-speed cruise. A minimum amount of 40% of laminar flow was required for cruise and high speed. Several geometric constraints were imposed by the structural requirements, the fuel-storage capability, and the constructing methodology.

Dedicated design tools have been developed by integrating 3-D geometry modification methods with aerodynamic codes and a stability analysis criterion. For the transition evaluation, the database method was adopted, which is able to evaluate both the Tollmien–Schlichting and crossflow instability progress, coupled with a boundary-layer analysis code based on the conical-flow assumption.

The principal design variables were the airfoil geometry, the thickness, and the twist distributions. Six sections were used to build the geometry, and a CAD constructing methodology was defined. A base airfoil was first designed using a quasi-3-D approach. The other sections were derived from the base geometry in such a way to accomplish local requirements (both aerodynamic and structural). Attention was devoted to the selection of the compromising twist distribution that, associated with a careful aileron region design, had to generate the appropriate stall pattern.

The 3-D iterative design process involved several cycles in which three methods were used for the performance evaluation. A full-potential method applied to a linear piecewise geometry defined by the six control sections was used in a first preliminary geometry definition. An Euler analysis coupled with the database method followed, to have a more accurate evaluation of the wave drag and to verify the stability properties of the boundary layer. The third phase involved the CAD model construction, the computational domain generation, and the Navier–Stokes analysis, with an imposed amount of laminar flow.

The final design evidenced an extension of more than 40% of laminar flow at cruise and at high speed. The target wave drag limit of 20 drag counts in high-speed cruising condition was respected, and all the structural and aerodynamic constraints were accomplished. A maximum lift coefficient of 1.3 at low speed was estimated.

A wind-tunnel test campaign at DNW-HST was carried out on a half-wing model at flight Reynolds number conditions. Several transition visualizations were performed using infrared cameras at design and offdesign conditions. The tests confirmed the capability of the wing to develop a wide stable region of laminar flow in all of the design points except in climb condition. Nevertheless, a region of premature transition was observed at the root region of the wing. A subsequent numerical investigation attributed this unexpected premature transition to small irregularities in the model geometry and

to the interference caused by the wing/fuselage configuration. In any case, the laminar flow showed to be able to tolerate moderate waviness on the surface.

Appendix A: Rule of Cosine

The validity of a two-dimensional analysis is restricted to the plane of an aerodynamic field in which the orthogonal gradients are zero. For this reason, the two-dimensional analysis of the airfoil section of a swept wing must refer to the so-called rule of cosine.

With the near-field approach, the total force that the fluid act on a generic body is given by [16]

$$F = \int_{S_{\text{body}}} [(P - P_\infty) \cdot n - (\tau \cdot n)] \, \mathrm{d}S \tag{A1}$$

where P is the static pressure and τ is the viscous stress tensor.

In the lift calculation, the viscous stress tensor component is neglected and the lift is obtained by integrating the pressure distribution around the body. Referring to a wing with infinite span and leading-edge sweep angle Λ, the freestream velocity vector V_∞ can be divided into the component orthogonal to the leading edge $V_\infty \cos\Lambda$ and the component $V_\infty \sin\Lambda$ parallel to the leading edge. Because the velocity component parallel to the leading edge of the wing causes only a skim of the flow in the spanwise direction, the only velocity component that contributes to the production of lift is $V_\infty \cos\Lambda$. For such a reason, the wing-section characteristics are obtained by a two-dimensional analysis of the airfoil obtained by projecting the airfoil AB on the plane orthogonal to the leading edge (Fig. A1).

The effective incidence α_{eff} of the airfoil AB' is given by

$$\tan\alpha_{\text{eff}} = \frac{V_\infty \sin\alpha}{V_\infty \cos\alpha \cos\Lambda} = \frac{\tan\alpha}{\cos\Lambda} \tag{A2}$$

or, for small angles of attack,

$$\alpha_{\text{eff}} \cong \frac{\alpha}{\cos\Lambda} \tag{A3}$$

The chord and the coordinates of the effective airfoil AB' are

$$C' = C\cos\Lambda; \qquad X' = X\cos\Lambda; \qquad Y' = Y \tag{A4}$$

The effective velocity component that concerns the profile AB' is

$$V_{\text{eff}}^2 = V_\infty^2(\sin^2\alpha + \cos^2\alpha\cos^2\Lambda) = V_\infty^2(1 - \cos^2\alpha\sin^2\Lambda) \tag{A5}$$

or, for small α,

$$V_{\text{eff}} = V_\infty \cos\Lambda \tag{A6}$$

Because the total lift must be independent of the airfoil that we refer to (Galileo's law), we can write

$$L = \tfrac{1}{2}\rho V_\infty^2 S C_l = \tfrac{1}{2}\rho V_{\text{eff}}^2 S C_{l_{\text{eff}}} \tag{A7}$$

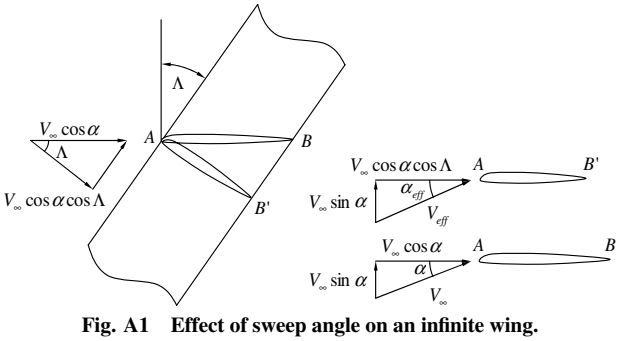

Fig. A1 Effect of sweep angle on an infinite wing.

from which we obtain

$$C_l = C_{l_{\text{eff}}} \frac{V_{\text{eff}}^2}{V_\infty^2} \tag{A8}$$

and finally, considering Eq. (A6),

$$C_l = C_{l_{\text{eff}}} \cos^2\Lambda \Rightarrow C_P = C_{P_{\text{eff}}} \cos^2\Lambda \tag{A9}$$

The effective Reynolds number is

$$Re_{\text{eff}} = \frac{V_{\text{eff}} C'}{\nu} = \frac{V_\infty \cos\Lambda C \cos\Lambda}{\nu} = \frac{V_\infty C}{\nu}\cos^2\Lambda = Re \cdot \cos^2\Lambda \tag{A10}$$

In the same manner, from Eq. (A6), the Mach number is

$$\text{Mach}_{\text{eff}} = \text{Mach} \cdot \cos\Lambda \tag{A11}$$

To calculate the drag of the wing section, the integral component of the viscous stress tensor can no longer be neglected.

The total drag of the wing section AB is given by

$$D = D_P + D_F \tag{A12}$$

where D_P is the pressure contribution and D_F is the skin-friction contribution.

Because, as already evidenced, only the $V_\infty \cos\Lambda$ component of the velocity contributes to the generation of the pressure distribution around the wing, the rule of cosine is applicable to estimate the pressure drag component of the wing from the analysis of the profile AB', treating it as it was done for the lift coefficient:

$$D_P = D_{P_{\text{eff}}} \cos\Lambda \Rightarrow C_{d_P} = C_{d_{P\text{eff}}} \cos^2\Lambda \cos\Lambda = C_{d_{P\text{eff}}} \cos^3\Lambda \tag{A13}$$

Within this method, it is not possible to get any information on the streamwise component of D_F from a two-dimensional analysis.

Acknowledgments

The authors wish to sincerely acknowledge Paolo Piscopo and Marco Di Vice for their significant contribution to the wind-tunnel model design and Mariano Manco and Aniello Menichino for their contribution to the model instrumentation, installation, and checking. A special thanks also goes to the personnel of the German–Dutch Wind Tunnel HST facility for their support during the test campaign.

References

[1] Schrauf, G., "Stability Analysis of the F100 Flight Experiment—A Second Look," Diamler-Benz Aerospace Airbus, ELFIN II Rept. 173, Bremen, Germany, Jan. 1996.

[2] Cella, U., Quagliarella, D., and Donelli, R., "Design and Optimisation of a Transonic Natural Laminar Flow Airfoil," Associazione Italiana Di Aeronautica e Astronautica 28th Congresso Nazionale, Sept. 2005.

[3] Drela, M., *A User's Guide to MSES 2.9*, MIT Computational Aerospace Sciences Lab., Cambridge, MA, Oct. 1995.

[4] Raymer, D. P., *Aircraft Design: A Conceptual Approach*, 3rd ed., AIAA Education Series, AIAA, Reston, VA, 1999.

[5] Roskam, J. and Lan, C.-T. E., "Airplane Aerodynamics and Performance," DARcorporation, Lawrence, KS, 1997.

[6] Iglesias, S. and Mason, W. H., "Optimum Spanloads Incorporating Wing Structural Weight," AIAA Paper 2001-5234, 2001.

[7] Nixon, D. (ed.), *Transonic Aerodynamics*, Progress in Astronautics and Aeronautics, Vol. 81, AIAA, Washington, D.C., 1981.

[8] Abbott, I. H., and Von Doenhoff, A. E., *Theory of Wing Sections*, Dover, Mineola, NY, 1959.

[9] Schlichting, H., *Boundary-Layer Theory*, McGraw–Hill Series in Mechanical Engineering, McGraw–Hill, New York, 1979.

[10] Kaups, K., and Cebeci, T., "Compressible Laminar Boundary Layers with Suction on Swept and Tapered Wings," McDonnell Douglas Astronautics Co., Rept. MDC J7337, St. Louis, MO, Sept. 1979.

[11] Perraud, J., Donelli, R. S., and Casalis, G., "Database Approach—Treatment of Stationary Mode," Application of Hybrid Laminar Flow Technology on Transport Aircraft (ALTTA), TR 24, Dec. 2001.

[12] Losito, V., *Fondamenti di Aeronautica Generale*, Accademia Aeronautica, Pozzuoli, Italy, 1991.
[13] Harris, C. D., "NASA Supercritical Airfoils," *A Matrix of Family-Related Airfoils*, NASA TP 2969, March 1990.
[14] Amato, M., Paparone, L., Catalano, P., and Puoti, V., "ZEN Flow Solver User Manual," Centro Italiano Ricerche Aerospaziali Rept. CIRA-UM-AEP-99-054, Capua, Italy, 1999.
[15] "The USAF Stability and Control DATCOM, Volume 1, Users Manual," McDonnell Douglas Astronautics Co., St. Louis, MO, April 1979.
[16] Tognaccini, R., *Methods for Drag Decomposition, Thrust-Drag Bookkeeping from CFD Calculations*, VKI Lecture Series 2003, von Karman Inst. for Fluid Dynamics, Rhode-St-Genèse, Belgium 2003.